SUPPORTING INFORMATION

Channelling Er^{3+}-Activated Vanadate Garnet's Multimode Luminescence for High-Sensitivity Optical Thermometers and NIR-II pc-LEDs for Bioimaging

Amrithakrishnan Bindhu[†]*, Jawahar I. Naseemabeevi, Subodh Ganesanpotti**

Department of Physics, University of Kerala, Kariavattom Campus, Thiruvananthapuram, Kerala - 695 581, India

Table S1 The ionic radii (D_r) percentage difference between host cations and Er^{3+}.

Host cation (CN)	**Doped ion (CN)**	**R_m (Å)**	**R_d (Å)**	**D_r (%)**
Sr^{2+} (8)	Er^{3+} (8)	1.26	1.004	20
Na^{+} (8)	Er^{3+} (8)	1.18	1.004	15
Mg^{2+} (6)	Er^{3+} (8)	0.72	1.004	-39
V^{5+} (4)	Er^{3+} (8)	0.355	1.004	-183

Table S2 Rietveld refinement and crystallographic parameters of $Sr_{1.8}Er_{0.10}Na_{1.1}Mg_2V_3O_{12}$.

Formula	**$Sr_{1.8}Er_{0.10}Na_{1.1}Mg_2V_3O_{12}$**
Crystal system	**Cubic**
Space group	***$Ia\bar{3}d$* (230, O_h^{10})**
Cell Parameter	***a=12.601(1) Å***
Reliability factors	**R_{wp}= 4.81%, R_p= 3.63% and GOF= 1.15**

Atom	Site	x	y	z	Occupancy	B_{eq} ($Å^2$)
Sr^{2+}/Er^{3+}	24c	0.375	0.5	0.25	0.667	0.009(5)
Na^{+}	24c	0.375	0.5	0.25	0.333	0.009(5)
Mg^{2+}	16a	0.50	0.50	0	1	0.008(1)
V^{5+}	24d	0.625	0.50	0.25	1	0.005(8)
O^{2-}	96h	0.039(8)	0.049(1)	0.653(6)	1	0.009(6)

Table S3 FIR (G_1/G_2) fitting parameters of SNMV: Er^{3+}.

FIR= A exp(-C/T) Adj. R^2 = 0.99961	
A	1.84591 ± 0.01965
C	567.09992 ± 3.41295

Table S4 FIR (G_1/R) fitting parameters of SNMV: Er^{3+}.

FIR= $A+BT+CT^2+DT^3$ Adj. R^2 = 0.99951	
A	0.27409 ± 0.01942
B	$-0.00612 \pm 3.04862\times10^{-4}$
C	$4.26362\times10^{-5} \pm 1.45152\times10^{-6}$
D	$-6.07438\times10^{-8} \pm 2.13701\times10^{-9}$

Table S5 FIR (R/G_2) fitting parameters of SNMV: Er^{3+}.

FIR= A+B exp(-C/T) Adj. R^2 = 0.986	
A	0.38793 ± 0.00292
B	3.03266 ± 0.70457
C	1206.5211 ± 89.39

Table S6 Temperature sensitivity comparison of reported phosphors based on the upconversion process.

Phosphors	Temperature (K)	S_r (%K^{-1})	Reference
$Na_2YMg_2(VO_4)_3$: Er/Yb	303	1.104	[1]
La_2MgTiO_6: Er	303	1.107	[2]
$Na_5Gd_9F_{32}$: Er	300	0.011	[3]
Y_2O_3: Yb/Er	150	5.28	[4]
$NaYF_4$: Ce/Tb/ Eu	563	1.17	[5]
$Cs_3GdGe_3O_9$: Er/Yb	303	1.224	[6]
$Cs_3GdGe_3O_9$: Er	313	1.27	[7]
$La_2Mo_2O_9$: Er	293	1.16	[8]
$NaYTiO_4$: Er/Yb/Sc	308	1.06	[9]
$Li_6CaLa_2Nb_2O_{12}$: Er/Yb	298	1.47	[10]
$Y_{4.67}(SiO_4)_3O$: Er/Yb	303	1.185	[11]
$La_{9.67}Si_6O_{26.5}$: Er/Yb	303	1.062	[12]
$K_3Y(PO_4)_2$: Yb/Er	303	1.228	[13]
$Na_{0.5}Gd_{0.5}MoO_4$: Yb/Er	590	0.856	[14]
$Bi_4Ti_3O_{12}$: Yb/Ho	323	2.11	[15]
Y_2O_3: Yb/Ho/Zn	299	0.302	[16]
$KLa(MoO_4)_2$: Yb/Tm	453	2.93	[17]
$NaLa(MoO_4)_2$: Er/Yb	450	1.3	[18]
$GdBiW_2O_9$: Er/Yb	300	1.2	[19]
$SrLaLiTeO_6$: Er^{3+}, Yb^{3+}	140	4.49	[20]
$Sr_2NaMg_2V_3O_{12}$: Er (R/G_2)	80	4.2	This work
$Sr_2NaMg_2V_3O_{12}$: Er (G_1/R)	100	3.1	This work

$Sr_2NaMg_2V_3O_{12}$: Er (G_1/G_2)	120	8.9	This work

Table S7 RPIR fitting parameters of SNMV: Er^{3+}.

FIR= $A+BT+CT^2+DT^3$ Adj. R^2 = 0.97988	
A	0.87424 ± 0.63652
B	-0.00304 ± 0.00387
C	$5.44788 \times 10^{-6} \pm 7.51178 \times 10^{-6}$
D	$-2.82908 \times 10^{-10} \pm 4.68331 \times 10^{-9}$

Table S8 Isotropic displacement parameters, U_{iso} of $Sr_2NaMg_2V_3O_{12}$.

Atom	U_{iso} (Å^2)
Sr^{2+}	0.00012(4)
Na^+	0.00012(4)
Mg^{2+}	0.0001(0)
V^{5+}	0.00007(7)
O^{2-}	0.00012(4)

Table S9 Fractional atomic coordinates, occupancy factors, isotropic displacement parameters, U_{iso} of $Sr_2NaMg_2V_3O_{12}$: Er^{3+}.

Atom	U_{iso} (Å^2)
Sr^{2+}	0.00012(0)
Na^{+}	0.00012(0)
Mg^{2+}	0.0001(0)
V^{5+}	0.00007(3)
O^{2-}	0.00012(1)

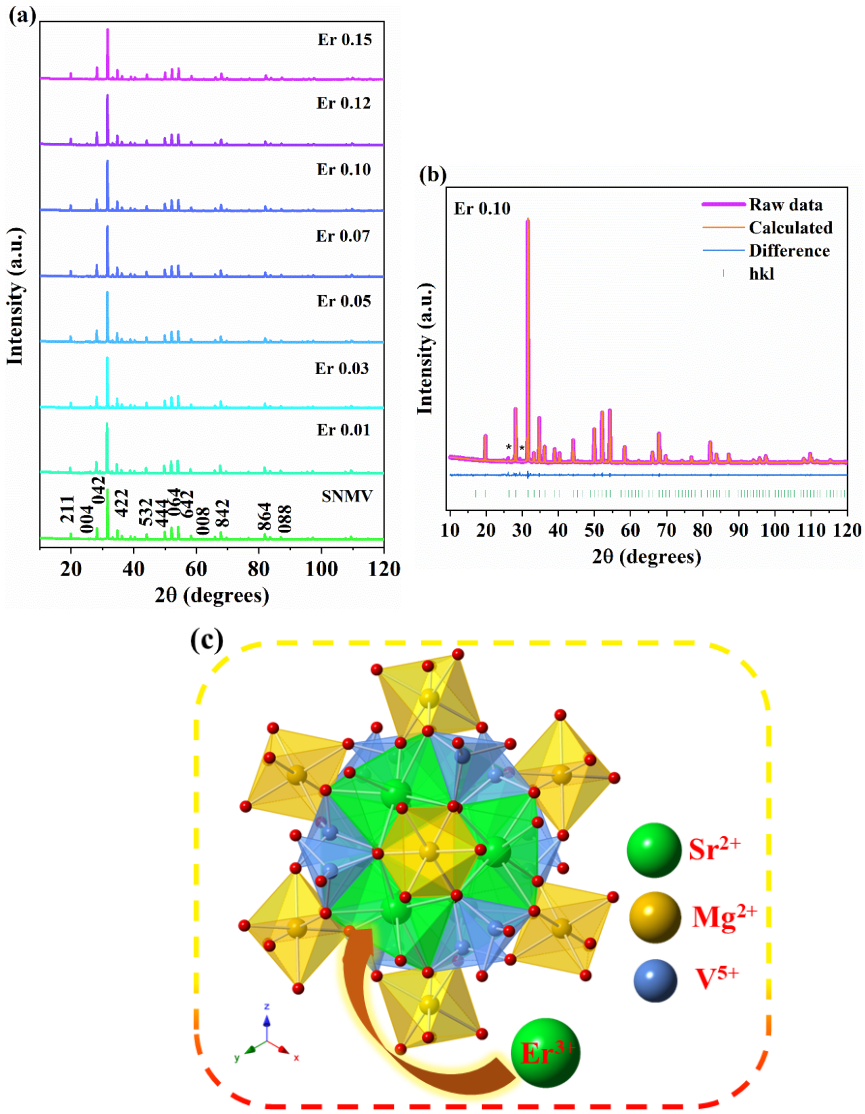

Figure S1 (a) XRD patterns of SNMV: Er (x=0, 0.01, 0.03, 0.05, 0.07, 0.10, 0.12 and 0.15) and (b) Rietveld refinement pattern of SNMV: 0.10 Er and (c) crystal structure viewed along 111 axis and schematic substitution of Er^{3+} into the dodecahedral site.

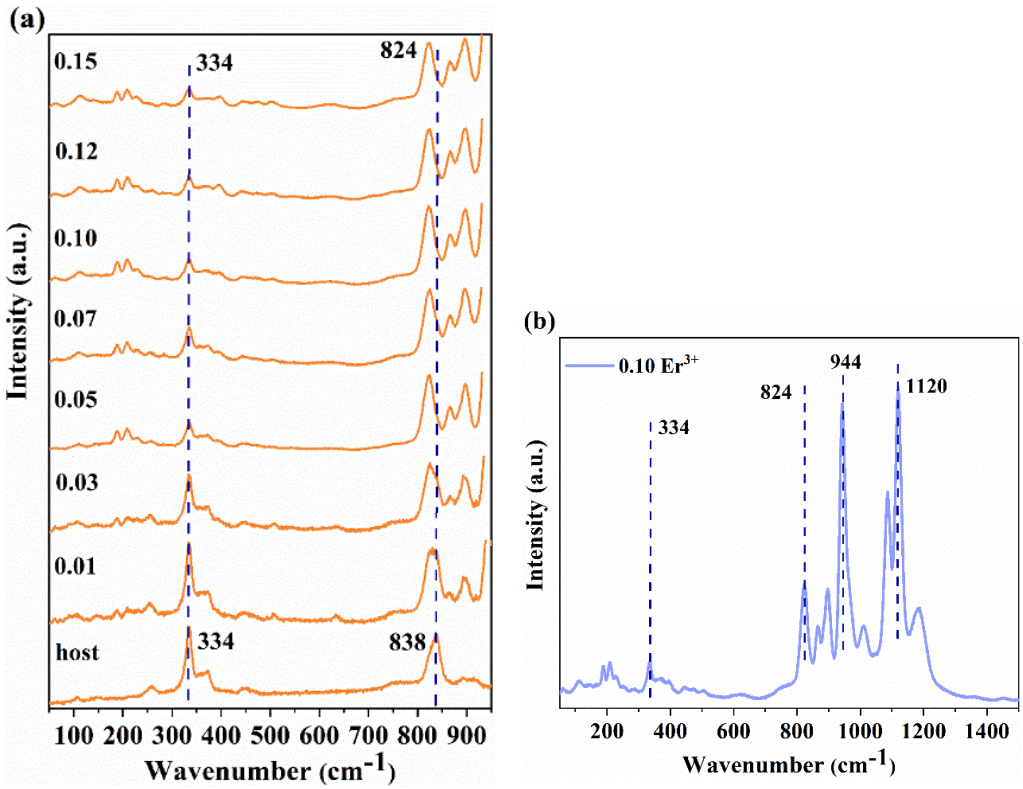

Figure S2 (a) Raman spectra of $Sr_2NaMg_2V_3O_{12}$: xEr^{3+} (x=0, 0.01, 0.03, 0.05, 0.07, 0.10 0.12, and 0.15), and (b) Raman spectra of SNMV: 0.10 Er^{3+} in the range 50-1500 cm^{-1}.

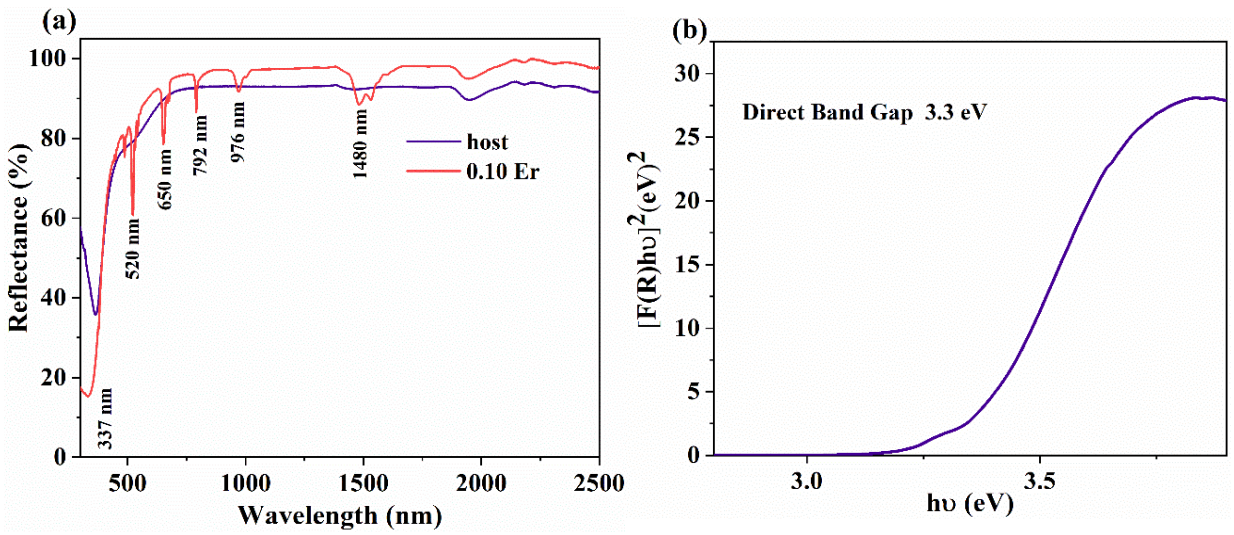

Figure S3 (a) The DRS spectra of SNMV host and SNMV: 0.10 Er^{3+} phosphors and (b) the bandgap calculated using the Kubelka-Munk function.

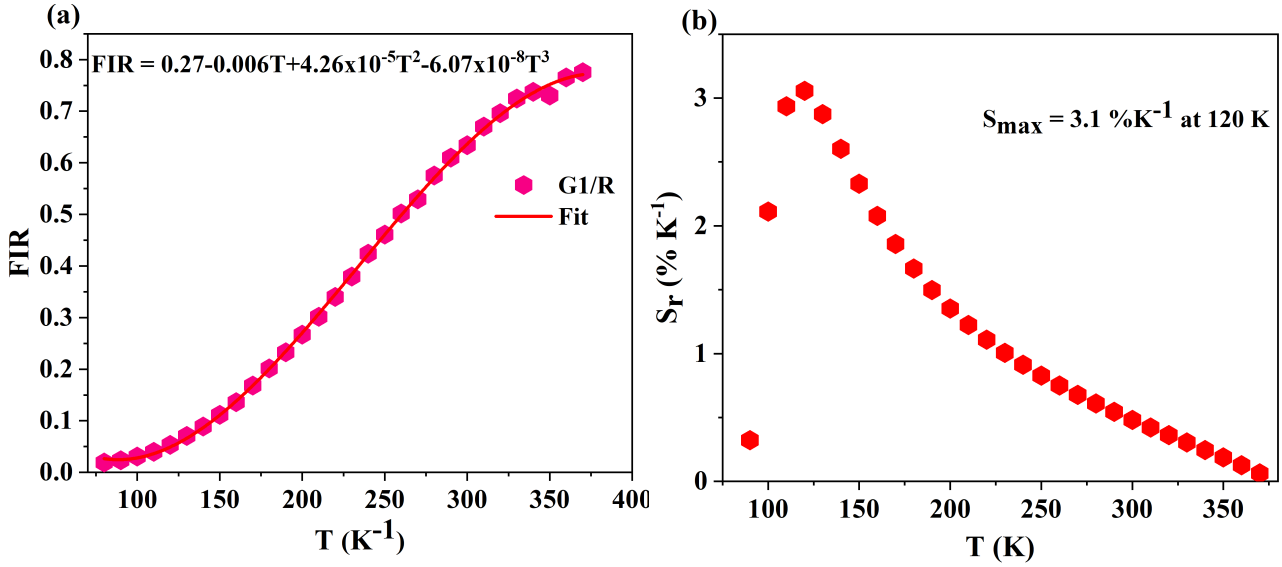

Figure S4 (a) The variation of (a) FIR- $\frac{I_{G1}}{I_R}$ and (b) S_r with T.

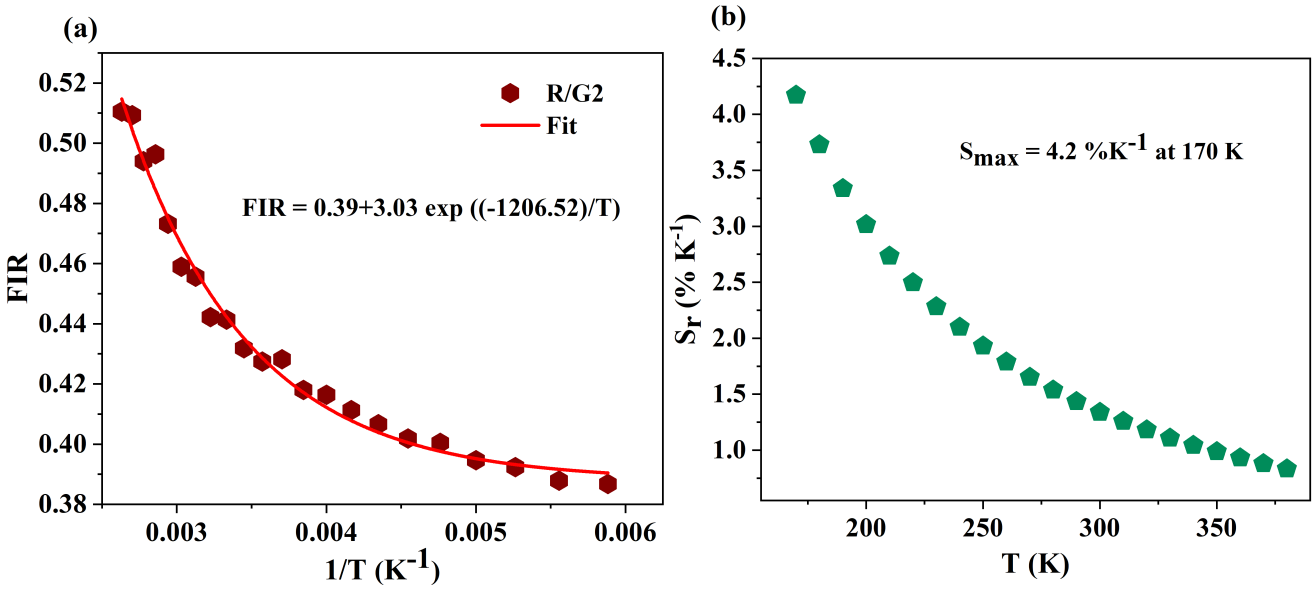

Figure S5 (a) The variation of (a) FIR- $\frac{I_R}{I_{G2}}$ and (b) S_r with T.

Down-shifting Photoluminescence

Figure S6(a) shows the excitation spectra of SNMV: xEr (x= 0.01, 0.03, 0.05, 0.07, 0.10, 0.12, and 0.15) monitoring at the intense 541 nm emission. Excitation spectra consist of a broad charge transfer band with maxima at 335 nm and characteristic 4f-4f transitions of Er^{3+} at 377 and 520 nm. The intense excitation band at 377 nm corresponds to the $^4I_{15/2} \rightarrow {}^4G_{11/2}$ transition. The broad excitation band is due to ligand to metal charge transfer (LMCT) transition from the *2p* orbital of O^{2-} to the *3d* orbital of V^{5+} ion. Thus, in the downshifting process, the VO_4^{3-} complex absorbs UV excitation energy and transfers this energy to the high energy states of Er^{3+} via the phonon-assisted energy transfer mechanism. Moreover, from the concentration-dependent PL spectra (Figure S6 (b)), the broad emission band of the VO_4^{3-} complex is overlapped with the transitions of Er^{3+}. The G_1 and R bands are diminished. However, the G_2 band is intense with maxima at 541 nm, corresponding to the transition $^4S_{3/2} \rightarrow {}^4I_{15/2}$. A decrease in the VO_4^{3-} band is noted with an increase in Er^{3+} concentration. Hence energy transfer from VO_4^{3-} complex to Er^{3+} has been associated with the downshifting process of the SNMV: Er system, resulting in green emission from Er^{3+} levels. The energy transfer efficiency is calculated using the relation,

$$\eta = 1 - \frac{I_s}{I_0} \% \quad (1)$$

where η is the energy transfer efficiency, I_s and I_0 are the emission intensities with and without Er^{3+}. A high energy transfer efficiency is observed in the Er^{3+} activated phosphors, in which 80% of efficiency is obtained for 0.10 Er SNMV phosphor (Figure S6 (c)). In addition, the CIE coordinates of the phosphor are evaluated under host excitation, as shown in the CIE diagram as shown in Figure S6 (d). A cyan emission with CIE coordinates (0.214, 0.351) is obtained due to the blue-green emission of the VO_4^{3-} complex and the green emission of Er^{3+} levels.

Apart from host excitation, the downshifting photoluminescence under f-f excitation of Er^{3+} is also carried out. The concentration-dependent photoluminescence spectra under the excitation 377 nm are shown in Figure S7 (a).

Similar to UCL and DSL under host excitation, the green bands exhibit strong emissions along with the broad emission of VO_4^{3-}. Nevertheless, the intensity of the broad emission of vanadate decreases owing to the excitation in the long wavelength region. The green bands, G_1 and G_2, are at 524 and 541 nm, whereas the red band, R, appears at 675 nm, respectively. However, the intensity of the G_1 and R bands are weak compared to UCL spectra under 976 nm excitation. Unlike the UC mechanism, where bi-photon absorption excites Er^{3+} sequentially to the upper $^4F_{7/2}$ state, here, under short wavelength excitation, 377 nm or 355 nm, direct excitation to the $^4F_{7/2}$ state takes place.[21] Further, non-radiative transitions via multi-phonon relaxation process, the population of TCLs $^4S_{3/2}$ and $^2H_{11/2}$ states occurs. This is followed by the green emission when most of the excited ions reach the ground state- $^4I_{15/2}$. Hence, only a few excited Er^{3+} reach the red-emitting $^4F_{9/2}$ state to cause red emission. This results in weaker red emission in the downshifting process. On the other hand, as discussed earlier, a different mechanism exists for populating the $^4F_{9/2}$ state via MPR and ETU. It can be seen from Figure S7 (b) that emission band intensity increases up to 0.10 Er, beyond which concentration quenching takes place. The CIE coordinate corresponding to optimum concentration is shifted towards the green region with CIE coordinate (0.273, 0.442) compared to excitation under 355 nm, as depicted in Figure S7 (c). This is because blue-green emission from the VO_4^{3-} complex is lower due to the transfer of excitation energy to Er^{3+} ions. Rare-earth ions have weak absorption in the UV region, whereas VO_4^{3-} can absorb UV efficiently and thus can transfer the absorbed energy to Er^{3+}. The critical distance of the SNMV: Er system is calculated based on Blasse's expression given by,[22]

$$R_c \approx 2\left(\frac{3V}{4\pi\chi_c N}\right)^{1/3} \quad (2)$$

where V, χ_c, and N is the unit cell volume, critical concentration, and a number of irreplaceable host cations associated with the unit cell. Based on the calculation, R_c is found to be 16.8 Å, which implies that exchange interaction is not responsible for concentration quenching. The concentration quenching is due to the multipole interaction between activator ions. The energy level diagram depicting down conversion via host excitation and Er^{3+} excitation is given in Figure S7 (d). Moreover, a decrease in decay time with an increase in Er^{3+} concentration is noted in which 0.10 Er has a decay time of 7.1μs monitored under 335 excitation and 541 nm emission, as shown in Figure S8. The decrease in decay time is due to increased nonradiative transitions at higher concentrations.

Temperature Sensing Properties

In addition, the temperature sensing properties of SNMV: Er based on the down-shifting process under host excitation and f-f excitation of Er^{3+} are studied. The temperature-dependent photoluminescence spectra, variation of FIR, and relative temperature sensitivity under host excitation of 335 nm are shown in Figure S9 (a)-(c). Both VO_4^{3-} and Er^{3+} bands at 495 and 541 nm decrease intensity with increased temperature due to the enhanced nonradiative relaxations taking place at elevated temperatures. FIR is calculated by taking the integrated intensities of the emission band of VO_4^{3-} with maxima at 495 nm and the G_2 band of Er^{3+} at 541 nm. FIR is fitted by equation 13. Relative temperature sensitivity increases with an increase in temperature and reaches a maximum of 1.06 $\%K^{-1}$ at 440 K.

CTB Edge from TDPLE spectra

Further, a pronounced red shift of the V-O charge transfer band is noted with temperature rise, as shown in the temperature-dependent excitation spectra in Figure S10 (a). CTB shift from 333 to 347 nm with the rise in temperature from 100 to 500 K. Similar shift of the CTB is noted in SNMV: Eu^{3+}/Sm^{3+} systems.[23] At the same time, an increase in the intensity of CTB is noted up to 200 K and decreases further, as shown in Figure S10 (b). However, the edge of CTB at 392 nm shows an increase in intensity with an increase in temperature. At higher temperatures, electrons occupy higher vibrational sub-levels of the electronic states via thermal population. The occupation of higher vibrational sublevels results in absorbing less amount of excitation energy to transition to higher states and causes redshift of the CTB.[24,25,26]

The diverse thermal response exhibited by CTB and the edge at 392 nm can be effectively used for temperature sensing based on the excitation intensity ratio, EIR. Thus EIR, ($\frac{I_{392}}{I_{333}}$) is calculated and fitted using equation 13. The variation of EIR and relative temperature sensitivity with temperature is shown in Figure S10 (c) and (d). Relative temperature sensitivity increases with temperature and reaches the maximum of 0.78 $\%K^{-1}$ at 380 K, then decreases further. Thus, both temperature-dependent variations in intensities can be employed for temperature sensing applications.

In short, comparing the dual mode of emission based on up-conversion and downshifting luminescence for optical thermometry, it can be seen that temperature sensing based on upconversion luminescence presents better temperature sensitivity. Moreover, the temperature sensing based on TCL levels, G_1 and R outperformed than non-TCLs based fluorescence intensity ratio method.

Similar negative thermal quenching of the G_1 band could be observed in up-conversion luminescence. However, population inversion cannot be achieved beyond 300 K due to the increase in the rate of multi-phonon relaxation. In the downshifting luminescence, the mechanism of populating the thermally coupled levels- $^2H_{11/2}$ and $^4S_{3/2}$ is entirely different. Here, population to these levels is made possible via directly exciting to higher states or phonon-assisted energy transfer from VO_4^{3-} to Er^{3+}. Analysing the excitation spectra, it is clear that a major part of the green emission is due to the phonon-assisted energy transfer from the host. Moreover, host emission is prone to fast thermal quenching. As shown in the temperature-dependent decay curves monitored at 495 nm emission and 335 excitations, it can be noted that a rapid decrement in decay time from 5.2 to 1.7 μs is noted with the rise in temperature from 300 to 500 K, as depicted in Figure S11. This rapid fall in decay time is due to the increase in non-radiative transitions associated with the host emission. This favours the generation of more phonons and follows phonon-assisted energy transfer from VO_4^{3-} to higher electronic states of Er^{3+}. Since $^2H_{11/2}$ is higher in energy than $^4S_{3/2}$, at elevated temperatures, the majority will occupy a higher state than lower $^4S_{3/2}$ in the downshifting process. Consequently, the G_1 band follows negative thermal quenching.

Thermochromic Luminescence Properties

Apart from thermometric properties, thermochromic properties of the SNMV: Er^{3+} system are also studied. The transit of CIE coordinates with temperature under various excitations is depicted in Figure S12 (a)-(c). Comparing the CIE coordinates, a pronounced shift in CIE coordinates from (0.214, 0.351) to (0.212, 0.553) is noted for the temperature rise from 300 to 500 K under 335 nm excitation. The shift in CIE coordinates under 335 nm excitation is due to the rapid quenching of VO_4^{3-} emission. However, UCL and DSL spectra under 976 and 377 nm, f-f excitation of Er^{3+},

exhibit only a slight shift in CIE coordinates. The fast thermal quenching of VO_4^{3-} is due to the enhancement in the nonradiative transitions via the cross-over mechanism.[24] The rapid shift from cyan to green emission of SNMV: Er^{3+} can be effectively utilized for safety sign applications in the high-temperature environment or as high-temperature alarms.

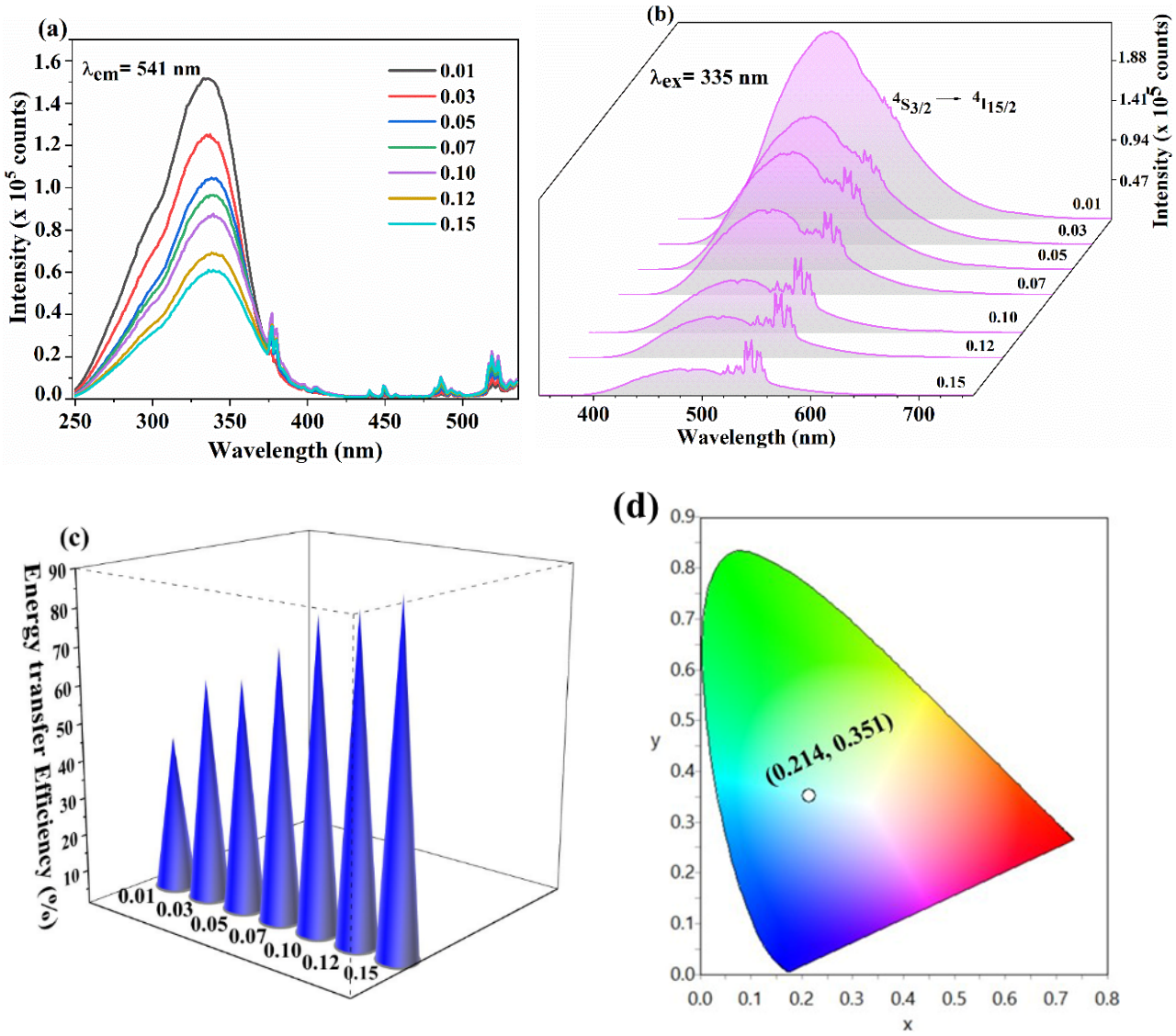

Figure S6 (a) The concentration-dependent PLE and (b) PL spectra of SNMV: xEr^{3+} (x= 0.01, 0.03, 0.05, 0.07, 0.10, 0.12 and 0.15) under host excitation of 335 nm, (c) energy transfer efficiency and (d) CIE diagram corresponding to 0.10 Er SNMV phosphor.

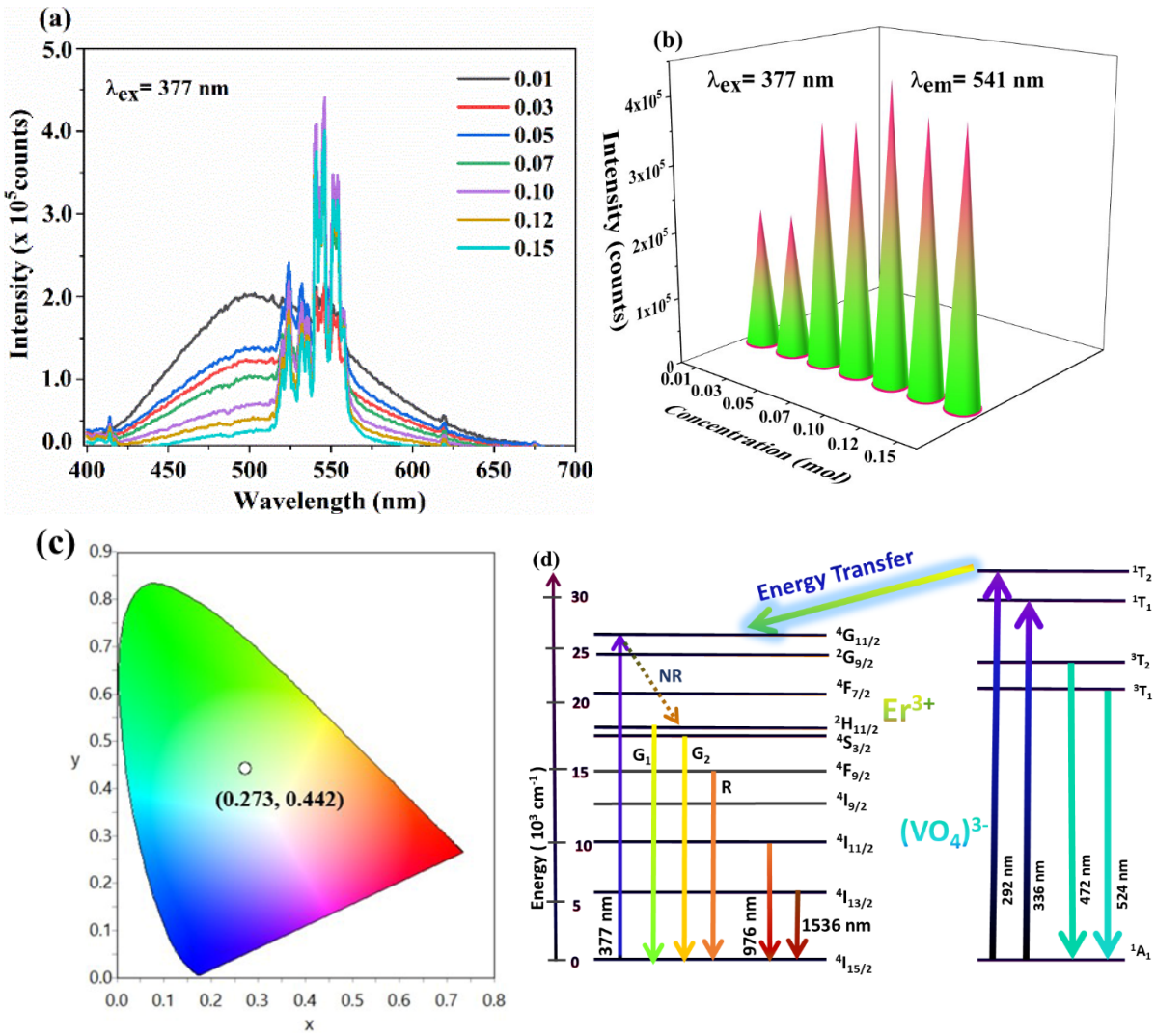

Figure S7 (a) Concentration-dependent PL spectra under 377 nm excitation, (b) variation of emission intensity with concentration, (c) CIE diagram corresponding to 0.10 Er phosphor, (d) Energy level diagram.

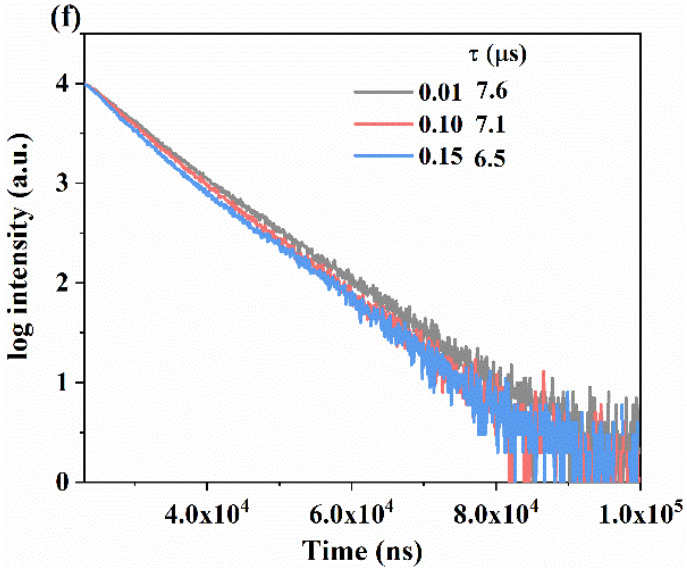

Figure S8 Decay curves of SNMV: 0.01, 0.10, and 0.15 Er phosphors.

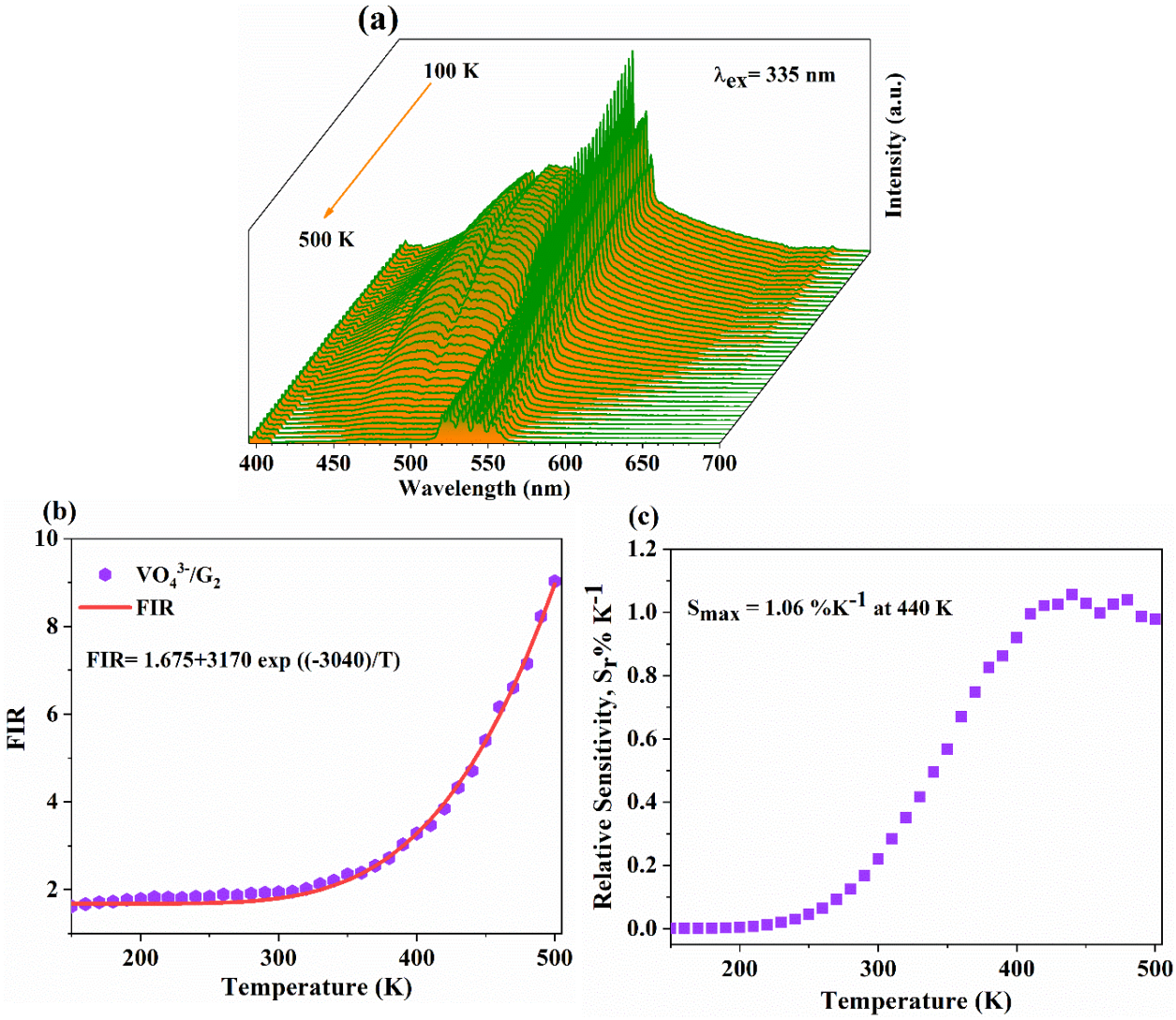

Figure S9 (a) Temperature-dependent DSL spectra of SNMV: 0.10 Er under host excitation of 335 nm, (b) variation of FIR, and (c) S_r with T.

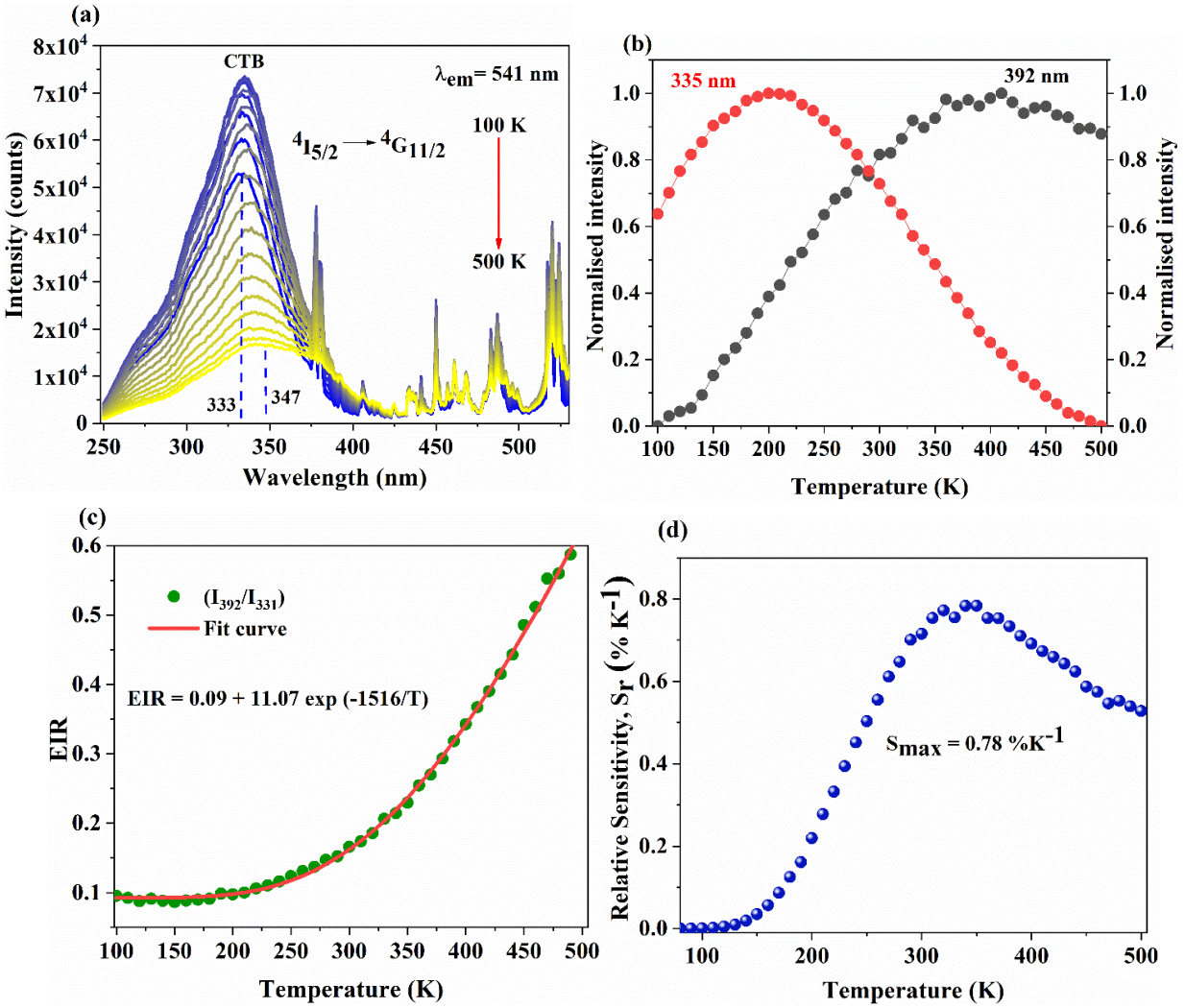

Figure S10 (a) The TDPLE spectra monitored under emission of 541 nm, (b) the variation in the intensity of CTB and CTB edge at 335 and 392 nm, respectively, (c) and (d) The variation of EIR and relative temperature sensitivity, S_r with temperature.

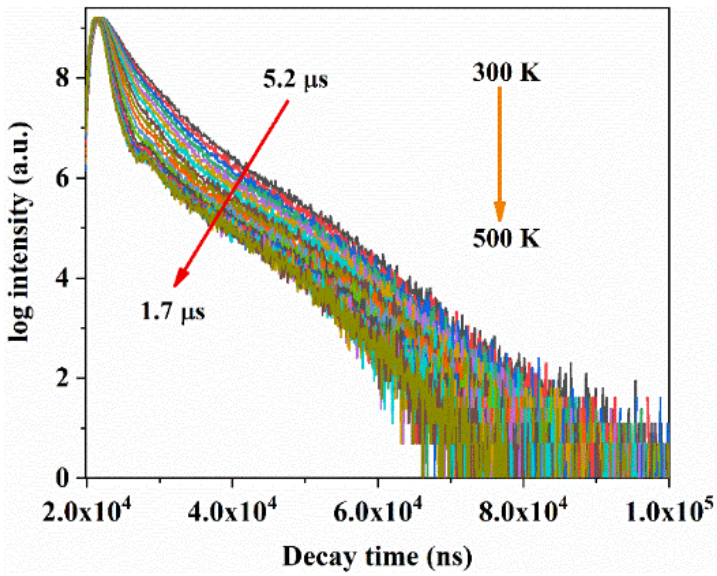

Figure S11 Temperature-dependent decay time analysis in the range 300-500 K.

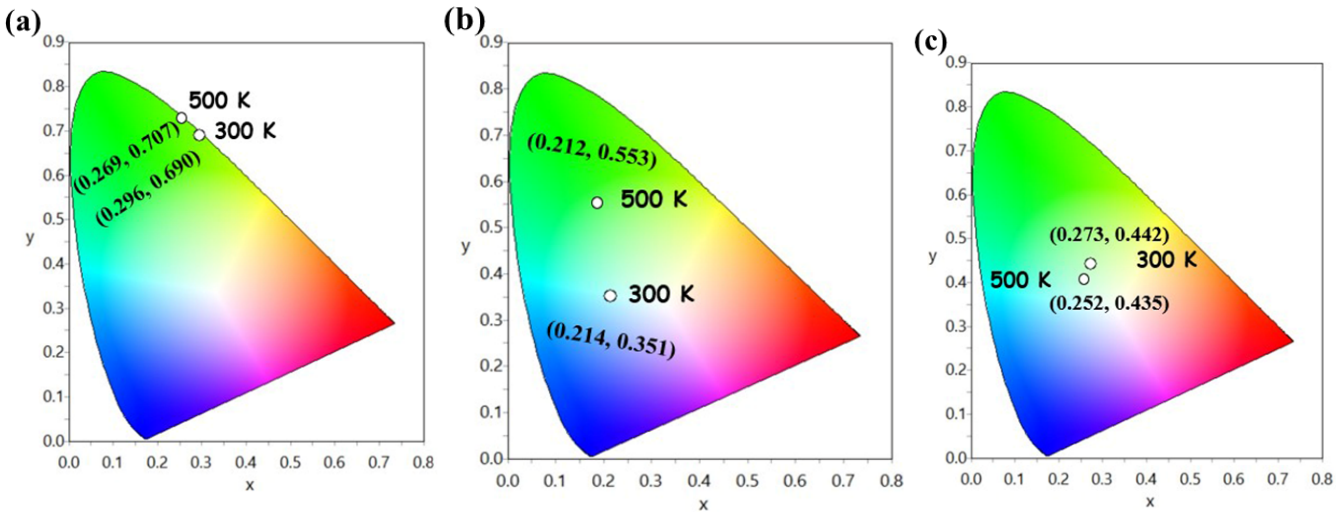

Figure S12 (a) Colorific shift in response to temperature for (a) UCL, (b) 335 nm, and (c) 377 nm.

REFERENCES

1. Y. Tong, W. N. Zhang, R. F. Wei, L. P. Chen, H. Guo, *Ceram Int* **2021**, *47*, 2600.

2. Y. Hua, J. S. Yu, *ACS Sustain Chem Eng* **2021**, *9*, 5105.

3. X. Li, J. Cao, F. Hu, R. Wei, H. Guo, *RSC Adv* **2017**, *7*, 35147.

4. V. Lojpur, G. Nikolić, M. D. Dramićanin, *J Appl Phys* **2014**, *115*, 203106.

5. M. Ding, M. Xu, D. Chen, *J Alloys Compd* **2017**, *713*, 236.

6. H. Cui, Y. Cao, L. Zhang, Y. Li, Y. Zhang, L. Li, J. Zhang, B. Chen, *Journal of the American Ceramic Society* **2023**, DOI 10.1111/JACE.18989.

7. R. Wei, F. Lu, L. Wang, F. Hu, X. Tian, H. Guo, *J Mater Chem C Mater* **2022**, *10*, 9492.

8. Y. Fan, Q. Xiao, X. Yin, L. Lv, X. Wu, X. Dong, M. Xing, Y. Tian, X. Luo, *Solid State Sci* **2022**, *132*, 106966.

9. Y. Wang, C. Zuo, C. Ma, W. Ye, C. Zhao, Z. Feng, Y. Li, Z. Wen, C. Wang, X. Shen, X. Yuan, Y. Cao, *J Alloys Compd* **2021**, *876*, DOI 10.1016/j.jallcom.2021.160166.

10. P. Du, X. Sun, Q. Zhu, J. G. Li, *Scr Mater* **2020**, *185*, 140.

11. J. Zhang, Y. Chen, G. Chen, *Opt Laser Technol* **2019**, *120*, DOI 10.1016/j.optlastec.2019.105747.

12. J. Zhang, J. Chen, Y. Zhang, *Inorg Chem Front* **2020**, *7*, 4892.

13. J. Zhang, Y. Zhang, X. Jiang, *J Alloys Compd* **2018**, *748*, 438.

14. P. Du, L. Luo, H. K. Park, J. S. Yu, *Chemical Engineering Journal* **2016**, *306*, 840.

15. Y. Huang, G. Bai, Y. Zhao, H. Xie, X. Yang, S. Xu, *Inorg Chem* **2020**, *59*, 14229.

16. M. M. Upadhyay, K. Kumar, *Journal of Rare Earths* **2022**, DOI 10.1016/J.JRE.2022.07.005.

17. Y. Zhang, B. Wang, Y. Liu, G. Bai, Z. Fu, H. Liu, *Dalton Transactions* **2021**, *50*, 1239.

18. D. He, C. Guo, S. Zhou, L. Zhang, Z. Yang, C. Duan, M. Yin, *CrystEngComm* **2015**, *17*, 7745.

19. S. Dutta, S. Som, T. M. Chen, *ACS Omega* **2018**, *3*, 11088.

20. P. Kaithrikkovil Varriam, S. Ganesanpotti, *Laser Photon Rev* **2024**, *18*, 2400245.

21. R. Bokolia, O. P. Thakur, V. K. Rai, S. K. Sharma, K. Sreenivas, *Ceram Int* **2015**, *41*, 6055.

22. G. Blasse, *Philips Research Reports* **1969**, *24*, 131.

23. A. Bindhu, J. I. Naseemabeevi, S. Ganesanpotti, *Mater Adv* **2023**, *4*, 3796.

24. A. Bindhu, J. I. Naseemabeevi, S. Ganesanpotti, *Adv Photonics Res* **2022**, *3*, 2100159.

25. S. Zhou, C. Duan, S. Han, *Dalton Transactions* **2018**, *47*, 1599.

26. D. Duan, Y. Wang, S. Jiang, L. Li, G. Xiang, X. Tang, Y. Li, X. Zhou, *J Lumin* **2019**, *215*, 116636.